GEOCHEMISTRY

Climate system asymmetries drive eccentricity pacing of hydroclimate during the early Eocene greenhouse

Andrew P. Walters[1]*, Jessica E. Tierney[1], Jiang Zhu[2], Stephen R. Meyers[3], Katherine Graves[1], Alan R. Carroll[3]

The early Eocene Climatic Optimum (EECO) represents the peak of Earth's last sustained greenhouse climate interval. To investigate hydroclimate variability in western North America during the EECO, we developed an orbitally resolved leaf wax δ^2H record from one of the most well-dated terrestrial paleoclimate archives, the Green River Formation. Our δ^2H_{wax} results show ~60‰ variation and evidence for eccentricity and precession forcing. iCESM simulations indicate that changes in the Earth's orbit drive large seasonal variations in precipitation and δ^2H of precipitation at our study site, primarily during the summer season. Our findings suggest that the astronomical response in δ^2H_{wax} is attributable to an asymmetrical climate response to the seasonal cycle, a "clipping" of precession forcing, and asymmetric carbon cycle dynamics, which further enhance the influence of eccentricity modulation on the hydrological cycle during the EECO. More broadly, our study provides an explanation for how and why eccentricity emerges as a dominant frequency in climate records from ice-free greenhouse worlds.

INTRODUCTION

The Early Eocene Climatic Optimum [EECO; approximately 53.3 to 49.1 million years (Ma)] (*1*), Earth's last greenhouse climate interval, is associated with the warmest sustained conditions of the Cenozoic, with global mean surface temperatures of ~27°C (*2*). This peak in the broader greenhouse climate state of the early Eocene resulted from a ~6 Ma secular rise in atmospheric CO_2 (*3*), which proxy records suggest culminated in concentrations of at least 1500 parts per million (*4*). Warm temperatures during the early Eocene were further enhanced by a series of transient, rapid hyperthermal events resulting from punctuated large-scale releases of greenhouse gases (*5*). At least 10 hyperthermals are hypothesized to have occurred during the EECO interval (*3*, *6*).

As the most recent example of a greenhouse climate state in Earth's history, the EECO is critical for improving our understanding of climate dynamics under extreme warm conditions. Much of our current understanding of the EECO—including the timing and magnitude of hyperthermal events—stems from detailed cyclostratigraphic, sedimentological, and geochemical analysis of marine cores (*3*, *5*, *7*–*11*). While indisputably valuable for understanding the impact of a warm climate on the world's oceans, marine records provide limited insight into continental responses. Terrestrial records can more suitably address a range of fundamental questions concerning continental responses to greenhouse conditions because they preserve a unique record of the interactions between climate, topography, landscapes, and biota.

The structure of the hydrological cycle on continents during the early Eocene greenhouse is one such key question; to date, the response of this component of the climate system under warm climate conditions remains loosely constrained, despite its clear impact on regional climate and landscape evolution. Climate simulations of the early Eocene broadly suggest an intensification of the hydrologic cycle; however, intermodel differences in the distribution of precipitation within the continents are large due to the high sensitivity of model results to paleoclimate boundary conditions and model parameterizations (*12*). This is compounded by a general lack of paleohydrologic proxy data for the Eocene after the Paleocene Eocene Thermal Maximum (PETM), because only a few studies have developed geochemical proxy records for hydrological change in the low and mid-latitudes (*13*–*16*). Furthermore, studies published to date typically lack sufficient sampling resolution and temporal control to investigate potential astronomical influences on continental hydrologic variability, despite evidence for the presence of orbital cycles in a diverse range of paleoclimate records from the early Eocene (*17*–*20*).

To investigate mid-latitudinal continental hydroclimate variability in western North America at the peak of the EECO greenhouse climate, we developed an orbitally resolved hydrogen isotope record from leaf wax *n*-acids (δ^2H_{wax}) sampled from the Wilkins Peak Member (WPM) of the Green River Formation in Wyoming (Fig. 1). This lacustrine unit, deposited at a paleolatitude of approximately 44.75°N in the Bridger sub-basin of the Greater Green River Basin (Fig. 1), is one of the richest and best-dated terrestrial stratigraphic archives of the early Eocene (*17*, *21*). Previous regional climate modeling of early Eocene western North America suggests that Lake Gosiute, the paleolake which deposited the WPM, may have received precipitation sourced from both the Pacific Ocean and the Gulf of Mexico (*22*, *23*). Moisture sourced from the Pacific Ocean is expected to have a more negative hydrogen isotope composition based on present-day observations of rainfall derived from these two potential sources (*24*). This difference in δ^2H_{precip} composition is due to temperature and evaporation influences at each source as well as differing degrees of isotopic fractionation as precipitation moves along moisture pathways from each source to Lake Gosiute (*25*, *26*).

Hydrogen isotope analysis of leaf waxes can be used to characterize this deep-time moisture source variability because long-chain

---

[1] Department of Geosciences, University of Arizona, Tucson, AZ 85721, USA. [2] Climate and Global Dynamic Laboratory, National Center for Atmospheric Research, Boulder, CO 80305, USA. [3] Department of Geoscience, University of Wisconsin-Madison, Madison, WI 53706, USA.
*Corresponding author. Email: apwalters@arizona.edu

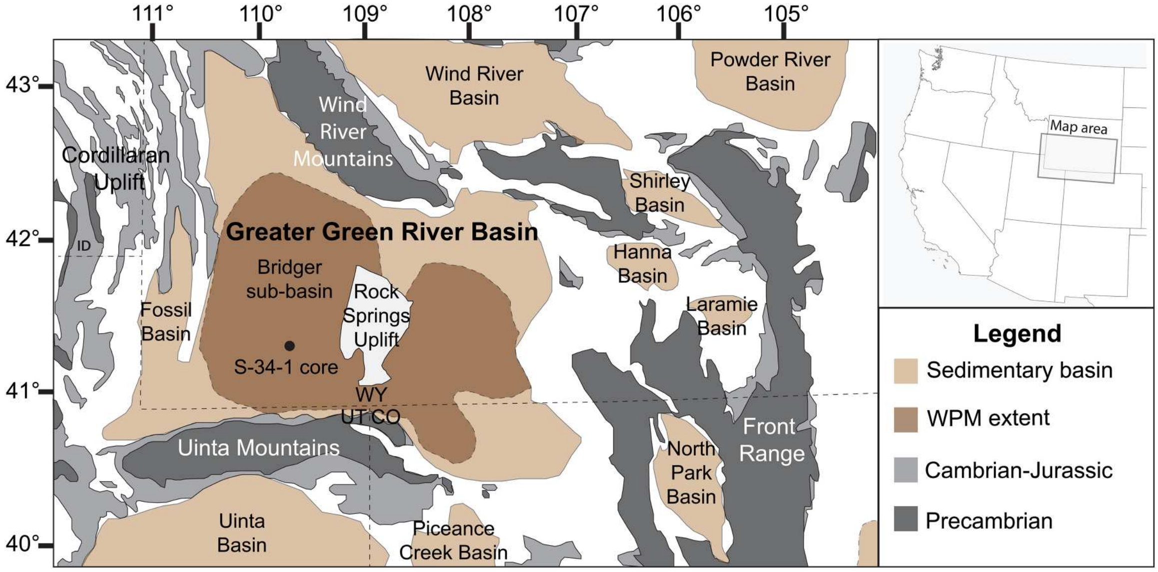

Fig. 1. Location of the Solvay S-34-1 core used in this study relative to regional geologic features. This core is located at 41.414231°N, 109.69675°W (WGS-84). The extent of the WPM, the unit sampled in this study, is shown in dark brown. Modified from (*21*, *83*).

(C_{24-32}) *n*-acids, which are predominantly produced by terrestrial plants (*27*), reflect the isotopic composition of local precipitation (*28*) and are chemically stable over geologic time scales (*29*). Specifically, we target the C_{30} *n*-acid for our measurements because this homolog is not known to be produced by other sources aside from terrestrial plants (whereas contributions from emergent aquatic plants and microbial sources have been reported for the C_{24-32} homologs) (*30*–*32*). The difference in isotopic composition between precipitation and leaf wax, termed the "apparent fractionation," can vary across different plant types and environments (*28*); however, we interpret our δ^2H_{wax} record to primarily reflect δ^2H_{precip} (Supplementary Materials). Furthermore, burial history reconstructions of the Greater Green River Basin indicate that the WPM has low thermal maturity (*33*), suggesting that the leaf wax *n*-acids evaluated in this study were not affected by burial diagenesis.

To complement this δ^2H_{wax} dataset, we developed a Bayesian age model of the WPM (fig. S1). This age model uses four high-precision U-Pb ages (table S1) (*34*) derived from volcanic tephra deposited in the WPM and makes no astronomical tuning assumptions. This temporal control, in combination with our densely sampled δ^2H_{wax} record [with a median sample resolution of 1.425 thousand years (ka)], provides the opportunity to investigate the patterns and time scales of variability in the Eocene hydrological cycle in unprecedented detail and resolution. These δ^2H_{wax} data are complemented by an analysis of water isotope-enabled climate simulations for the early Eocene to elucidate the drivers of hydroclimate variability in western North America during the EECO.

RESULTS

Variations in δ^2H_{wax}

Our 196 temporally calibrated δ^2H_{wax} measurements from the WPM span approximately 343,000 years of the peak EECO greenhouse interval, between 51.35 (±0.171) Ma and 51.01 (±0.202) Ma (Fig. 2A). Within our record, we observe δ^2H_{wax} values as enriched as −121‰ and as depleted as −188‰, a range of more than 60‰ (Fig. 2A). In addition to this large-scale, long-term variation, we observe multimillennial-scale variations of ~10 to 20‰ throughout the record (Fig. 2A).

Power spectral analysis of our δ^2H_{wax} record shows the frequency distribution of variance within this dataset (Fig. 2B and fig. S2) and identifies significant astronomical-scale variability relative to an AR1 stochastic null model (fig. S2). We identify the largest peak in power at ~0.01 cycles/ka (period = 100 ka; Fig. 2B), which is consistent with short-eccentricity cyclicity and is statistically significant at the conventional 99% confidence level (fig. S2). In addition, the 94.88 ka short eccentricity cycle predicted by a key theoretical astronomical solution (*35*) has a 99.8% robust AR1 Bonferroni-corrected confidence level for the periodogram and 97.6% robust AR1 Bonferroni-corrected confidence level for the multitaper method (MTM). Evolutive harmonic analysis (EHA) (*36*) of our δ^2H_{wax} record shows a large, continuous peak in power and amplitude at this frequency across most of the record (fig. S3). The 343 ka duration of our hydrogen isotope record does not permit detection of the long eccentricity (405 ka) cycle directly, but we observe a frequency and amplitude modulation of the short eccentricity signal (Fig. 3 and fig. S3), which is indicative of the presence of a long eccentricity cycle (*37*). Past cyclostratigraphic analysis of the WPM also reported evidence of eccentricity-scale variations in the sedimentation and lake level (*17*, *38*, *39*) that are consistent with our δ^2H_{wax} data. Application of bandpass filtering (*40*) to extract the eccentricity signal shows that this ~100 ka cycle in δ^2H_{wax} is associated with long-term, high-amplitude isotopic variation of up to 25‰ in our dataset (Fig. 3).

We also observe power concentrated at frequencies that are nominally in the precession band (*35*), including a prominent peak at 0.0444 cycles/ka (period = 22.5 ka) and additional peaks at 0.0407 cycles/ka (period = 24.5 ka) and 0.0617 cycles/ka (period = 16.2 ka) (Fig. 2B). Each of these precession band peaks in power exceeds the AR1 spectral background (fig. S2), with several exceeding the conventional 90% confidence level (fig. S2). However, the 22.57 and

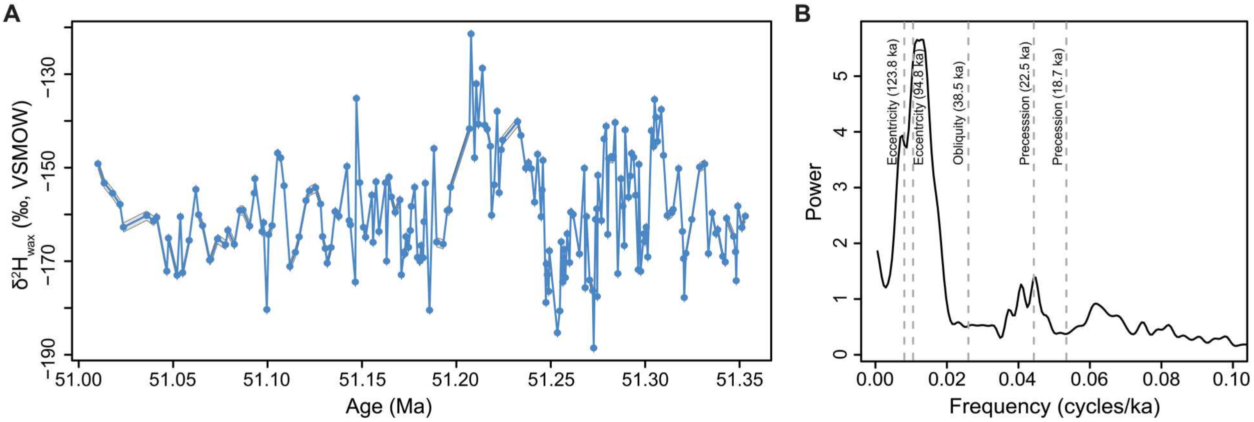

Fig. 2. Variations in leaf wax δ^2H across the EECO-age WPM. (**A**) Temporally calibrated δ^2H_{wax} values (blue circles) with average 1σ analytical uncertainty (gray shading). (**B**) MTM power spectra (*74*) [3-2π discrete prolate spheroidal sequence (DPSS) tapers] results for these δ^2H_{wax} data, with vertical gray dashed lines highlighting the five main astronomical cycles predicted by theoretical astronomical solutions (*35*). In (B), the data were linearly detrended before analysis.

18.72 ka precession periods predicted for this record by the La04 theoretical astronomical solution (*35*) do not achieve the 90% Bonferroni-corrected confidence level (fig. S2). This lack of a significant precession signal may be due to sedimentation rate instability that is not accounted for in the age model, which is known to preferentially distort higher frequency cycles (Fig. 2B; Supplementary Materials) (*36*). In addition, there is uncertainty in the predicted periods for precession for the early Eocene (*35*). While precession-scale variability in δ^2H_{wax} is of lower magnitude, it is associated with discernible variations of up to 16‰ (Fig. 3). Notably, we do not detect power associated with obliquity (period = 38.46 ka) (Fig. 2B) (*35*) despite the mid-latitude paleolocation of Lake Gosiute. In total, the eccentricity to precession frequency band accounts for more than 71% of the variance in the δ^2H_{wax} record and is associated with isotopic variations of approximately 40‰ (Fig. 3).

Simulations of early Eocene hydroclimate

To provide context for our δ^2H_{wax} data and decipher the drivers of changes in precipitation and precipitation isotopes at Lake Gosiute, we analyze early Eocene model simulations conducted with the water isotope-enabled Community Earth System Model (iCESM) (*41*). While climate simulations for the early Eocene show large intermodel differences in precipitation amount and distribution in the mid-latitudes (*12*, *42*), the CESM model has shown a close agreement with a variety of proxy-derived climate reconstructions for the Eocene (*41*–*43*), which lends confidence in the ability of this model to simulate large-scale changes in the hydrological cycle. These iCESM simulations were conducted at 3× and 6× preindustrial concentrations of CO_2 with DeepMIP boundary conditions (*44*). First, we evaluate changes in the annual cycle of precipitation amount and δ^2H of precipitation delivered to Lake Gosiute across two end-member astronomical configurations under 3× CO_2 levels, termed "OrbMaxN" and "OrbMaxS." OrbMaxN is configured with high eccentricity (0.054), obliquity (24.5°), and the precessional perihelion in the northern hemisphere summer, effectively maximizing the seasonal variations in insolation at our northern hemisphere paleolake. In contrast, OrbMaxS is configured with high eccentricity, obliquity, and the precessional perihelion in the southern hemisphere summer, resulting in more moderate seasonal changes in insolation at our mid-latitude northern hemisphere paleolake.

The simulations reveal major differences in the seasonal cycle of precipitation between these two astronomical configurations (Fig. 4). OrbMaxS shows a gradual transition in the amount of precipitation delivered to Lake Gosiute, moving from a relatively drier winter season to wetter late spring, summer, and early fall seasons and then back to a drier winter season (Fig. 4A). In contrast, OrbMaxN results in slightly drier winters, sharper seasonal transitions into and out of the wetter seasons, and two separate peaks in precipitation centered in May and September (Fig. 4A).

On the basis of these results, summer appears to be the key season in which the difference in the amount of precipitation received at Lake Gosiute between the two astronomical configurations is greatest (Fig. 4A). Looking at how this difference between OrbMaxN and OrbMaxS configurations is distributed spatially across western North America, we observe several features that elucidate the physical processes associated with this astronomically driven precipitation variation (Fig. 4B). Near the Pacific Ocean, OrbMaxN conditions intensify the proto–North American monsoon relative to OrbMaxS, but little of the precipitation resulting from this enhanced hydrologic system travels over Cordilleran uplift to Lake Gosiute, given the elevation of this range in paleotopographical reconstructions (fig. S4) (*45*–*47*). Instead, OrbMaxN produces drier summer and fall conditions over the Front Range east and southeast of Lake Gosiute, as well as over the Gulf of Mexico (Fig. 4B). The overall pattern of a stronger proto–North American monsoon accompanied by dry conditions over west-central North America in our Eocene simulations is consistent with proxy and modeling evidence from the Holocene, which shows similar astronomically driven changes associated with the position and strength of the subtropical highs and westerly winds (*48*, *49*).

The annual cycle of δ^2H of precipitation delivered to Lake Gosiute in our early Eocene simulations also shows key differences between the OrbMaxN and OrbMaxS configurations (Fig. 4C). In both cases, Lake Gosiute receives more isotopically depleted precipitation in the winter and more enriched precipitation in the summer, which reflects the distinctive seasonal moisture sources

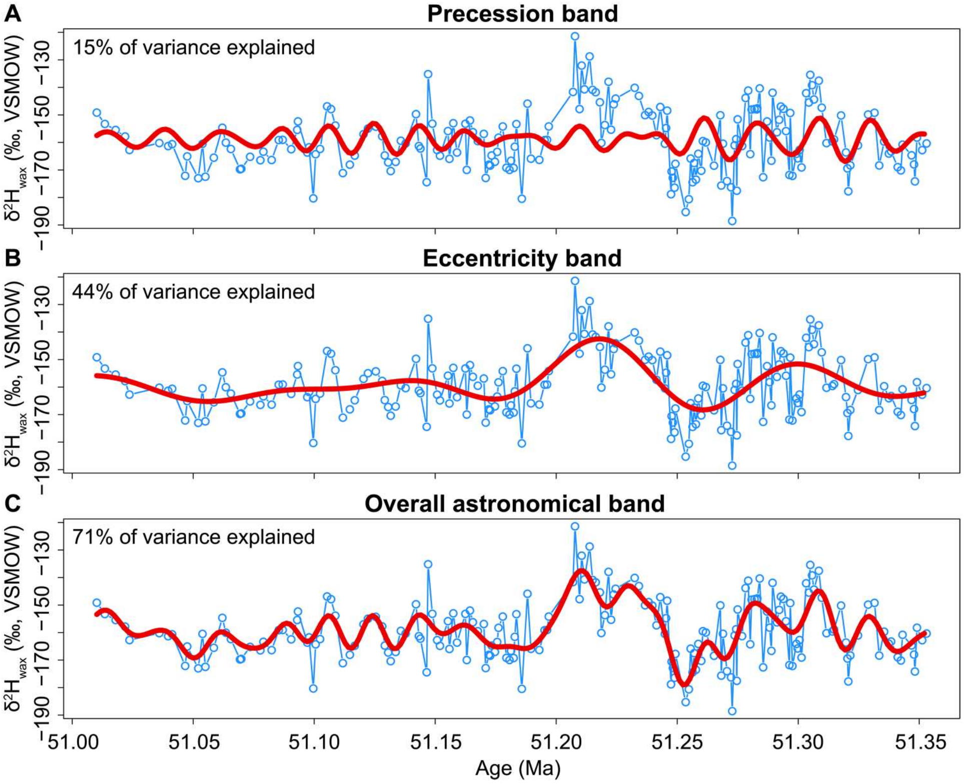

Fig. 3. Taner bandpass filtering of the δ^2H_{wax} record. Taner filter results (in red) for (**A**) precession, (**B**) eccentricity, and (**C**) the overall astronomical band are compared to the δ^2H_{wax} data (in blue). Filter parameters are included in Materials and Methods.

(Fig. 4C). However, OrbMaxN results in an enhanced seasonal range in δ^2H_{precip} when compared to OrbMaxS, with a 50‰ difference between the winter and summer season compared to a 30‰ difference in OrbMaxS (Fig. 4C). As with precipitation amount, the difference in δ^2H_{precip} between these two astronomical configurations is largest during the summer season. Across western North America, summer moisture and precipitation is broadly enriched in OrbMaxN, especially along the Cordilleran uplift (Fig. 4D).

DISCUSSION

Our δ^2H_{wax} results suggest that precession and eccentricity influenced the hydrosphere of western North America at the peak of the early Eocene greenhouse climate (Fig. 3). These results are consistent with previous analysis of C_{29} *n*-alkanes in three cores from the Uinta Basin (fig. S5) (*16*), an adjoining basin of the Green River Formation south of our study site (Fig. 1). Although these Uinta Basin records were deposited later in the EECO, they show a similar ~−50 to 60‰ range of variation, with two of the three core locations also showing δ^2H_{wax} values comparable to our record (fig. S5) (*16*). The sampling resolution of this previous study was insufficient to evaluate potential orbital-scale influences on δ^2H_{wax}; however, the proximity of the Uinta Basin to our study site and the similar values of δ^2H_{wax} composition and variation suggest that the Uinta Basin may have been similarly influenced by precession and eccentricity.

The results of our early Eocene iCESM simulations further support these findings, indicating that changes in orbital configuration can drive corresponding changes in the annual cycle of precipitation and isotopes of precipitation at Lake Gosiute (Fig. 4). In addition, analysis of these simulations also illuminates the physical processes by which summer moisture and precipitation can become so highly enriched across the western North America region under particular orbital configurations (such as OrbMaxN), producing the more positive summer δ^2H_{precip} values simulated for our Lake Gosiute study site.

One explanation for this regional enrichment of precipitation across western North America is the strong land- and elevation-enhanced warming in summer temperature over the North America caused by the orbital forcing (fig. S6). Enhanced warming over land and at higher elevations acts to increase the saturation vapor pressure, resulting in less rain-out along the moisture transport pathway and more deuterium-enriched precipitation. The particularly enriched values simulated along the Cordilleran uplift (Fig. 4D) in OrbMaxN are consistent with this mechanism, as more enriched vapor would be able to travel further inland to form precipitation over this major regional high.

Changes in moisture sourcing in this region of the North American continent represent a second explanation for the regional enrichment. In response to OrbMaxN forcing, summer temperatures increase in the Northern Hemisphere and the subtropical highs strengthen, resulting in an overall warmer and drier continental interior. In addition, low-level wind anomalies suggest that there was a relative increase in the amount of precipitation sourced from the Gulf of Mexico, contributing to more positive δ^2H_{precip} at Lake Gosiute (fig. S6). Quantifying the relative contributions of these two processes (land- and elevation-enhanced warming versus

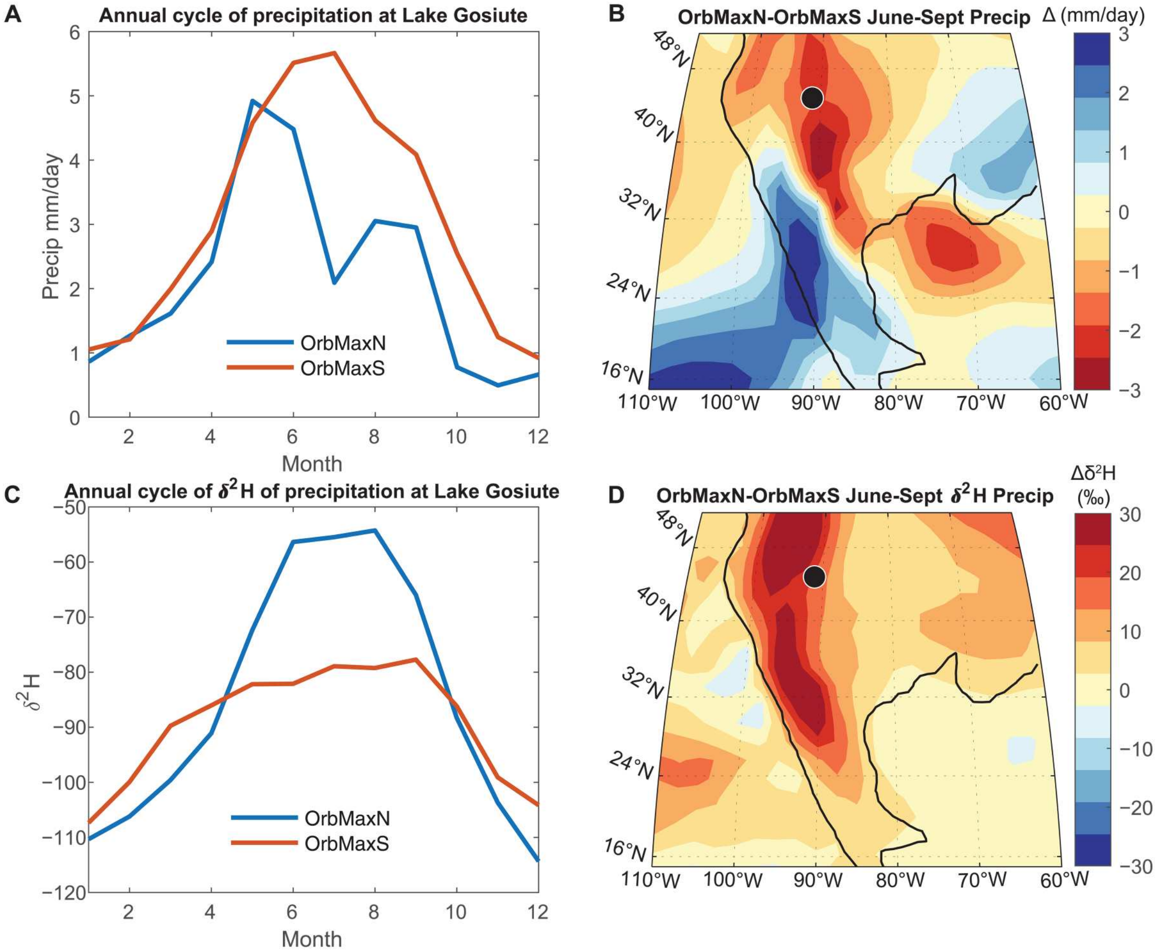

Fig. 4. Eocene iCESM simulation results for precipitation amount and δ^2H of precipitation. (**A**) Annual cycle of precipitation at Lake Gosiute. (**B**) Difference in summer precipitation amount between OrbMaxN and OrbMaxS configurations across western North America. (**C**) Annual cycle of hydrogen isotopes of precipitation at Lake Gosiute. (**D**) Difference in summer hydrogen isotope composition between OrbMaxN and OrbMaxS configurations across western North America. (A) and (C) Site values for Lake Gosiute are calculated by averaging within a 2° × 2° box around the location of the Solvay S-34-1 core. (B) and (D) The dot indicates the location of the Solvay S-34-1 core.

changes in moisture sources) would require additional simulations and is out of the scope of the present study; nevertheless, it is likely that both of these processes drove isotopic enrichment of precipitation at Lake Gosiute.

These simulations also shed light on the mechanisms by which precession and eccentricity signals can be expressed in our δ^2H_{wax} results. Although precession modulates the amplitude of the seasonal cycle, it has no net effect on mean annual insolation; therefore, the presence of a precession signal in our δ^2H_{wax} dataset indicates that a seasonally asymmetric climatic response (*50*) dominates annual mean δ^2H_{precip} variability. Our modeling results indicate that summer is the key season for maximizing the difference in precipitation amount and isotopes of precipitation to Lake Gosiute across different astronomical configurations (Fig. 4), supporting this hypothesis. Annual-mean δ^2H_{precip} at Lake Gosiute is dominated by changes in summer precipitation (the rainy season); changes occurring during the winter season simply have less of an impact on the annual-mean δ^2H_{precip} because conditions are much drier (Fig. 4A). Although we cannot rule out the additional possibility that δ^2H_{wax} is also seasonally biased toward to the rainy season [as has been argued for the PETM (*51*)], the modeling results suggest that this is not necessary to explain the presence of precession.

Given the large signal of eccentricity in our δ^2H_{wax} record relative to precession, despite eccentricity's comparatively minor influence on insolation variation (*35*), it is also necessary to consider the climatic and depositional mechanisms that serve to transfer power from precession to its modulation periods attributable to eccentricity. One possible mechanism is carbon cycle dynamics. Modeling has revealed that the residence time of carbon can produce a transfer of power from precession to eccentricity (*18*, *52*). Given this mechanism and clear evidence for eccentricity-paced hyperthermal events during the EECO (*3*, *5*, *6*), it is possible that western North American hydroclimate responded strongly to elevated CO_2 during hyperthermals, providing an avenue to generate an enhanced eccentricity signal in our δ^2H_{wax} record.

A second potential mechanism to transfer of power from precession to eccentricity is "clipping" of the precession signal (*53*–*55*). This process occurs when the climate system responds asymmetrically to insolation variations, i.e., below a threshold, the atmosphere or land surface responds too weakly to leave a signature in the geologic record for a substantial portion of the precession cycle, and/or the sedimentary system is not sufficiently sensitive to deposit across the full range of climatic variation associated with a precession cycle. As a result of this clipping, precessional variance is muted, while power is transferred to eccentricity as a result of the modulation of precession by eccentricity (*54*).

Our modeling results support the hypothesis that changes in the carbon cycle can influence the hydrologic system of Lake Gosiute, with a change from 3× to 6× preindustrial CO_2 levels—on the scale of what might occur during a hyperthermal event—generating an increase in δ^2H_{precip} of about 15‰ in the summer (Fig. 5). Given the ample evidence for eccentricity pacing of early Eocene hyperthermals (*5*, *56*–*59*), it is plausible that the hydrologic cycle of Lake Gosiute was, at times, strongly governed by CO_2 changes, which overrode precession-driven regional insolation variations and produced a stronger eccentricity signal in our δ^2H_{wax} record than predicted by astronomical theory. On the basis of our simulations, however, this mechanism is only able to account for part of the ~40‰ of variation observed in our δ^2H_{wax} dataset on astronomical time scales, suggesting that other processes may be acting to transfer power to eccentricity.

The remainder of the δ^2H_{wax} on astronomical time scales (ca. 25‰) may be attributable to our second hypothesized mechanism for transferring precessional power to eccentricity—clipping. The response of precipitation and the isotopes of precipitation to OrbMaxN is not symmetrical with OrbMin (low eccentricity and obliquity), with eccentricity maxima corresponding with isotopic enrichment and a drier summer (fig. S7). The muted response of the hydrological cycle to OrbMin conditions effectively "clips" the expression of insolation variation, allowing the summer-dominated precessional response to transfer into eccentricity variations.

While our modeling results suggest that neither CO_2 nor astronomical forcing can individually drive changes in δ^2H_{precip} at Lake Gosiute that match the magnitude seen in our proxy record, when considered together their predicted changes of 15 and 25‰ respectively add up to the 40‰ variation observed in our δ^2H_{wax} data on astronomical time scales. This suggests that astronomical and CO_2 forcings acted together to shape the hydroclimate of western North America during the EECO, and highlights how nonlinearities in the expression of both of these drivers result in an enhanced eccentricity signal.

Overall, our temporally calibrated, orbitally resolved δ^2H_{wax} record from the WPM of the Green River Formation, in tandem with our water isotope-enabled climate simulations, provides key insights into the behavior of the hydrologic cycle on continents during the EECO. We find the first evidence of astronomical forcing of North American hydroclimate during this greenhouse climate, paced by precession and short eccentricity. These emerge as a result of climate system asymmetries in the form of a larger response to summer insolation forcing and clipping processes, which produce prominent precession and short eccentricity cycles, as well as carbon cycle dynamics (i.e., hyperthermals), which are also asymmetric because the climate system responds only to increases in CO_2. Although clipping has been invoked previously to explain the emergence of 100 ka power at equatorial latitudes (*53*) and during the ice ages (*60*), our study shows that it can also emerge in the mid-latitudes under greenhouse climate conditions, simply due to nonlinear climate responses to astronomical forcing. Our study provides an interpretive framework for understanding the emergence of precession and eccentricity frequencies in paleoclimate. In particular, the asymmetric responses we identify here explain why eccentricity cycles are a ubiquitous presence in many deep-time proxy records from warm climates, despite the absence of ice-related feedback mechanisms (*5*, *18*, *37*, *57*, *61*–*65*). In addition, the preeminence of orbital forcing in our data suggest that the hydroclimate of other past greenhouse intervals is likely also paced by orbital cycles, but that high-resolution studies are needed to resolve this variability.

MATERIALS AND METHODS

Sample preparation and analysis

For detailed methods regarding the leaf wax analyses, we refer the reader to the Supplementary Materials. Briefly, we analyzed leaf wax hydrogen isotopes in 196 samples taken from the WPM of the

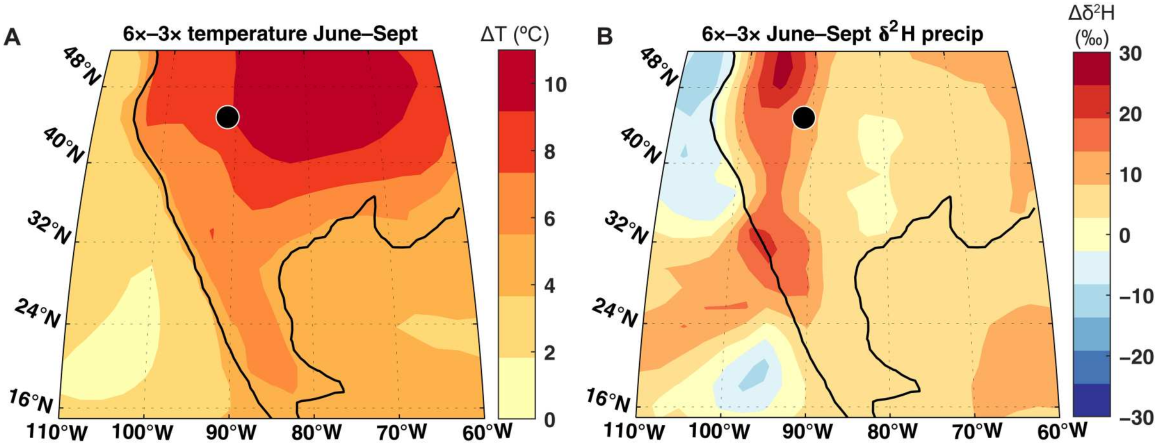

Fig. 5. Influence of different CO_2 concentrations on summer temperature and summer δ^2H of precipitation in Eocene iCESM simulations of western North America. (**A**) Differences in summer 2 m air temperature between 6× and 3× CO_2 simulations. (**B**) Differences in summer hydrogen isotopic composition of precipitation between 6× and 3× CO_2 simulations. The orbital configuration in these two simulations is fixed (i.e., set to preindustrial conditions). Dots indicate the location of the Solvay S-34-1 core.

Green River Formation, from the Solvay S-34-1 drill core (41.414231°N, 109.69675°W). Sample surfaces were thoroughly cleaned, and then samples were crushed to a powder using a cast-iron mortar and pestle. Total lipid extracts were extracted from ~10 g of sediment using a Thermo Scientific DIONEX ASE 350 accelerated solvent extractor system and a 9:1 ratio of dichloromethane: methanol. Activated copper powder was used to remove any elemental sulfur, and then column chromatography was performed to isolate the fatty acids. The fatty acid fraction was methylated overnight, and the resulting fatty acid methyl esters (FAMEs) were extracted using liquid-liquid extraction and then further purified via column chromatography.

Gas chromatography on a Thermo Scientific Trace 1310 GC was used to determine the distributions and concentrations of long-chain fatty acids present within the samples. FAMEs were analyzed for their deuterium/hydrogen (D/H) ratios on a Thermo Scientific Delta V Plus stable isotope mass spectrometer coupled to a Thermo Scientific Trace 1310 GC, Thermo Scientific Conflo IV, and Thermo Scientific GC Isolink II. Values of δ^2H_{wax} are reported as per mil versus Vienna Standard Mean Ocean Water. Following previous work (*66*–*71*), we measured D/H ratios specifically on the C_{30} *n*-acid as representative compound derived from higher plants (see the main text and Supplementary Materials). Standard error of duplicate or triplicate measurements averaged 0.98‰ across all samples. Data and analytical uncertainties are available in the data tables archived in the publicly accessible National Oceanic and Atmospheric Administration (NOAA) National Centers for Environmental Information (NCEI) Paleoclimatology database (https://ncei.noaa.gov/access/paleo-search/study/38021).

Spectral analysis and evaluation of statistical significance

Spectral analysis was conducted using the Astrochron (*72*) package for the R statistical program (*73*), using two approaches to quantify oscillatory variability in the data: the periodogram and MTM spectral analysis (*74*). Before spectral analysis, the δ^2H_{wax} data series was interpolated (piecewise-linear) to the median sampling interval (1.425 ka) using the Astrochron function "linterp."

Significance testing was completed using a robust AR1 stochastic null model (*75*, *76*), which was applied to the periodogram using the "periodogram" function in Astrochron and to the MTM spectrum using the "mtmML96" function in Astrochron (fig. S2). We calculated the conventional confidence levels used in astrochronology and paleoclimatology (*77*), and supplemented this with a multiple-testing procedure using the Bonferroni correction, to better guard against false positives. Because our dataset had a time scale that was independent of astrochronologic assumptions, we were able to use the Bonferroni multiple-testing correction to explicitly correct the confidence levels at the five main predicted astronomical cycles: the 94.88 and 123.84 ka eccentricity cycles, the 38.46 ka obliquity cycle, and the 22.57 and 18.73 ka precession terms, as determined using the La04 theoretical astronomical solution (*35*).

To further characterize cyclic variability, EHA—a method that implements MTM in a moving window—was applied using the "eha" function in Astrochron (*36*, *72*). This method was especially useful to visualize changes in power, amplitude, and frequency associated with a given cycle across the dataset.

Taner bandpass filtering of the data was completed using the "taner" function in Astrochron. A low-frequency half power point of 0.035 cycles/ka, a high-frequency half power point of 0.062 cycles/ka, and a roll off rate of 108 were used for the precession band (Fig. 3A). A low-frequency half power point of 0.001 cycles/ka, a high-frequency half power point of 0.016 cycles/ka, and a roll off rate of 108 were used for the eccentricity band (Fig. 3B). A low-frequency half power point of 0.000 cycles/ka, a high-frequency half power point of 0.065 cycles/ka, and a roll off rate of 108 were used for the overall astronomical band (Fig. 3C).

Age modeling

An age-depth model for our leaf wax isotope record was developed applying Bayesian statistical methods using the "rbacon" package (*78*) for R. This time model was constrained using four tuffs spanning the section, which have been dated using U-Pb methods by (*34*): the Firehole tuff (589.06 m), Second tuff (556.02 m), Boar tuff (515.47 m), and Grey tuff (481.61 m). This model was created using an "acc.shape" parameter of 1.2, an "acc.mean" parameter of 6500, and a "thick" parameter of 5.25 to optimize the accumulation rate prior for the range of accumulation rates typically observed in the Green River Formation (*21*). The Bayesian model indicated an average 2-σ age uncertainty of 0.166 Ma.

Climate model simulations

Climate model simulations were conducted with the fully coupled, isotope-enabled Community Earth System Model 1.2 (iCESM1.2) (*79*, *80*) with a horizontal resolution of 1.9° × 2.5° (latitude × longitude) in the atmosphere and land, and a nominal 1° displaced-pole Greenland grid for the ocean. The base Eocene simulations, with different CO_2 concentrations (3×, 6×, and 9× preindustrial levels), were previously presented and described in (*41*, *81*). These simulations used early Eocene boundary conditions from DeepMIP (*44*), which include Eocene paleogeography, land-sea mask, and vegetation distribution from (*45*), and preindustrial non-CO_2 greenhouse gas concentrations, solar constant, orbital parameters, soil properties, and natural aerosol emissions. These base simulations were run for 2200 years to reach quasi-equilibrium in the upper ocean. We then branched three different experiments off the 3× CO_2 Eocene baseline to examine different orbital configurations. Following the approach of (*82*), we conducted a minimum eccentricity and obliquity experiment (eccentricity = 0.0, obliquity = 22°; "OrbMin"), a high Northern Hemisphere seasonality scenario (eccentricity = 0.054, obliquity = 24.5°, perihelion during boreal summer; "OrbMaxN"), and a high Southern Hemisphere seasonality scenario (eccentricity = 0.054, obliquity = 24.5°, perihelion during austral summer; "OrbMaxS"). These experiments were each run for 500 years. We feature OrbMaxN-OrbMaxS differences in the main text because this maximizes the seasonal differences at our site; results for OrbMaxN-OrbMin are similar (fig. S7).

Supplementary Materials

This PDF file includes:
Supplementary Materials and Methods
Table S1
Figs. S1 to S7
References

REFERENCES AND NOTES

1. C. J. Hollis, T. Dunkley Jones, E. Anagnostou, P. K. Bijl, M. J. Cramwinckel, Y. Cui, G. R. Dickens, K. M. Edgar, Y. Eley, D. Evans, G. L. Foster, J. Frieling, G. N. Inglis, E. M. Kennedy, R. Kozdon, V. Lauretano, C. H. Lear, K. Littler, L. Lourens, A. N. Meckler, B. D. A. Naafs, H. Pälike,

R. D. Pancost, P. N. Pearson, U. Röhl, D. L. Royer, U. Salzmann, B. A. Schubert, H. Seebeck, A. Sluijs, R. P. Speijer, P. Stassen, J. Tierney, A. Tripati, B. Wade, T. Westerhold, C. Witkowski, J. C. Zachos, Y. G. Zhang, M. Huber, D. J. Lunt, The DeepMIP contribution to PMIP4: Methodologies for selection, compilation and analysis of latest Paleocene and early Eocene climate proxy data, incorporating version 0.1 of the DeepMIP database. *Geosci. Model Dev.* **12**, 3149–3206 (2019).

2. G. N. Inglis, F. Bragg, N. J. Burls, M. J. Cramwinckel, D. Evans, G. L. Foster, M. Huber, D. J. Lunt, N. Siler, S. Steinig, J. E. Tierney, R. Wilkinson, E. Anagnostou, A. M. de Boer, T. Dunkley Jones, K. M. Edgar, C. J. Hollis, D. K. Hutchinson, R. D. Pancost, Global mean surface temperature and climate sensitivity of the early Eocene Climatic Optimum (EECO), Paleocene-Eocene Thermal Maximum (PETM), and latest Paleocene. *Clim. Past* **16**, 1953–1968 (2020).
3. J. C. Zachos, G. R. Dickens, R. E. Zeebe, An early Cenozoic perspective on greenhouse warming and carbon-cycle dynamics. *Nature* **451**, 279–283 (2008).
4. J. W. Rae, Y. G. Zhang, X. Liu, G. L. Foster, H. M. Stoll, R. D. M. Whiteford, Atmospheric CO_2 over the past 66 million years from marine archives. *Annu. Rev. Earth Planet. Sci.* **49**, 609–641 (2021).
5. S. Kirtland Turner, P. F. Sexton, C. D. Charles, R. D. Norris, Persistence of carbon release events through the peak of early Eocene global warmth. *Nat. Geosci.* **7**, 748–751 (2014).
6. V. Lauretano, F. Hilgen, J. Zachos, L. Lourens, Astronomically tuned age model for the early Eocene carbon isotope events: A new high-resolution $\delta^{13}C_{benthic}$ record of ODP Site 1263 between ~49 and ~54 Ma. *Newsl. Stratigr.* **49**, 383–400 (2016).
7. G. R. Dickens, Rethinking the global carbon cycle with a large, dynamic and microbially mediated gas hydrate capacitor. *Earth Planet. Sci. Lett.* **213**, 169–183 (2003).
8. A. J. Ridgwell, Interpreting transient carbonate compensation depth changes by marine sediment core modeling. *Paleoceanography* **22**, 1–10 (2007).
9. K. Panchuk, A. Ridgwell, L. R. Kump, Sedimentary response to Paleocene-Eocene Thermal Maximum carbon release: A model-data comparison. *Geology* **36**, 315–318 (2008).
10. R. E. Zeebe, J. C. Zachos, G. R. Dickens, Carbon dioxide forcing alone insufficient to explain Palaeocene–Eocene Thermal Maximum warming. *Nat. Geosci.* **2**, 576–580 (2009).
11. D. E. Penman, S. K. Turner, P. F. Sexton, R. D. Norris, A. J. Dickson, S. Boulila, A. Ridgwell, R. E. Zeebe, J. C. Zachos, A. Cameron, T. Westerhold, U. Röhl, An abyssal carbonate compensation depth overshoot in the aftermath of the Palaeocene-Eocene Thermal Maximum. *Nat. Geosci.* **9**, 575–580 (2016).
12. M. J. Carmichael, D. J. Lunt, M. Huber, M. Heinemann, J. Kiehl, A. LeGrande, C. A. Loptson, C. D. Roberts, N. Sagoo, C. Shields, P. J. Valdes, A. Winguth, C. Winguth, R. D. Pancost, A model–model and data–model comparison for the early Eocene hydrological cycle. *Clim. Past* **12**, 455–481 (2016).
13. E. G. Hyland, N. D. Sheldon, Coupled CO_2-climate response during the Early Eocene Climatic Optimum. *Palaeoclim. Palaeoecol.* **369**, 125–135 (2013).
14. E. Hyland, N. D. Sheldon, M. Fan, Terrestrial paleoenvironmental reconstructions indicate transient peak warming during the early Eocene Climatic Optimum. *GSA Bull.* **125**, 1338–1348 (2013).
15. G. N. Inglis, M. J. Carmichael, A. Farnsworth, D. J. Lunt, R. D. Pancost, A long-term, high-latitude record of Eocene hydrological change in the Greenland region. *Palaeogeogr. Palaeoclimatol. Palaeoecol.* **537**, 109378 (2020).
16. A. L. Elson, M. Rohrssen, J. Marshall, G. N. Inglis, J. H. Whiteside, Hydroclimate variability in the United States continental interior during the early Eocene Climatic Optimum. *Palaeogeogr. Palaeoclimatol. Palaeoecol.* **595**, 110959 (2022).
17. W. Aswasereelert, S. R. Meyers, A. R. Carroll, S. E. Peters, M. E. Smith, K. L. Feigl, Basin-scale cyclostratigraphy of the Green River Formation, Wyoming. *Geol. Soc. Am. Bull.* **125**, 216–228 (2013).
18. R. E. Zeebe, T. Westerhold, K. Littler, J. C. Zachos, Orbital forcing of the Paleocene and Eocene carbon cycle. *Paleoceanography* **32**, 440–465 (2017).
19. V. Lauretano, J. C. Zachos, L. J. Lourens, Orbitally paced carbon and deep-sea temperature changes at the peak of the early Eocene climatic optimum. *Paleoceanogr. Paleoclimatology* **33**, 1050–1065 (2018).
20. T. Westerhold, U. Röhl, B. Donner, J. C. Zachos, Global extent of early Eocene hyperthermal events: A new Pacific benthic foraminiferal isotope record from Shatsky Rise (ODP Site 1209). *Paleoceanogr. Paleoclimatology* **33**, 626–642 (2018).
21. M. E. Smith, A. R. Carroll, B. S. Singer, Synoptic reconstruction of a major ancient lake system: Eocene Green River Formation, western United States. *Geol. Soc. Am. Bull.* **120**, 54–84 (2008).
22. M. Huber, R. Caballero, Eocene El Niño: Evidence for robust tropical dynamics in the "hothouse". *Science* **299**, 877–881 (2003).
23. J. O. Sewall, L. C. Sloan, Come a little bit closer: A high-resolution climate study of the early Paleogene Laramide foreland. *Geology* **34**, 81–84 (2006).
24. J. Hou, W. J. D'Andrea, Y. Huang, Can sedimentary leaf waxes record D/H ratios of continental precipitation? Field, model, and experimental assessments. *Geochim. Cosmochim. Acta* **72**, 3503–3517 (2008).
25. H. Craig, Isotopic variations in meteoric waters. *Science* **133**, 1702–1703 (1961).
26. J. R. Gat, Oxygen and hydrogen isotopes in the hydrologic cycle. *Annu. Rev. Earth Planet. Sci.* **24**, 225–262 (1996).
27. G. Eglinton, R. J. Hamilton, Leaf epicuticular waxes. *Science* **156**, 1322–1335 (1967).
28. D. Sachse, I. Billault, G. J. Bowen, Y. Chikaraishi, T. E. Dawson, S. J. Feakins, K. H. Freeman, C. R. Magill, F. A. McInerney, M. T. J. van der Meer, P. Polissar, R. J. Robins, J. P. Sachs, H. L. Schmidt, A. L. Sessions, J. W. C. White, J. B. West, A. Kahmen, Molecular paleohydrology: Interpreting the hydrogen-isotopic composition of lipid biomarkers from photosynthesizing organisms. *Annu. Rev. Earth Planet. Sci.* **40**, 221–249 (2012).
29. A. Schimmelmann, A. L. Sessions, M. Mastalerz, Hydrogen isotopic (D/H) composition of organic matter during diagenesis and thermal maturation. *Annu. Rev. Earth Planet. Sci.* **34**, 501–533 (2006).
30. S. Kusch, J. Rethemeyer, E. Schefuß, G. Mollenhauer, Controls on the age of vascular plant biomarkers in Black Sea sediments. *Geochim. Cosmochim. Acta* **74**, 7031–7047 (2010).
31. L. Gao, J. Hou, J. Toney, D. MacDonald, Y. Huang, Mathematical modeling of the aquatic macrophyte inputs of mid-chain *n*-alkyl lipids to lake sediments: Implications for interpreting compound specific hydrogen isotopic records. *Geochim. Cosmochim. Acta* **75**, 3781–3791 (2011).
32. S. J. Feakins, T. I. Eglinton, P. B. deMenocal, A comparison of biomarker records of northeast African vegetation from lacustrine and marine sediments (ca. 3.40 Ma). *Org. Geochem.* **38**, 1607–1624 (2007).
33. R. C. Johnson, J. E. Birdwell, T. J. Mercier, M. E. Brownfield, "Geology of tight oil and potential tight oil reservoirs in the lower part of the Green River Formation, Uinta, Piceance, and Greater Green River Basins, Utah, Colorado, and Wyoming" (Technical Report, U.S. Geological Survey, 2016).
34. B. T. Bruck, B. S. Singer, M. D. Schmitz, A. R. Carroll, S. Meyers, A. P. Walters, B. R. Jicha, Astronomical and tectonic influences on climate and deposition revealed through radioisotopic geochronology and Bayesian age-depth modeling of the early Eocene Green River Formation, Wyoming, USA. *GSA Bulletin* 2023; DOI:https://doi.org/10.1130/B36584.1.
35. J. Laskar, P. Robutel, F. Joutel, M. Gastineau, A. C. M. Correia, B. Levrard, A long-term numerical solution for the insolation quantities of the Earth. *Astron. Astrophys.* **428**, 261–285 (2004).
36. S. R. Meyers, B. B. Sageman, L. A. Hinnov, Integrated quantitative stratigraphy of the Cenomanian-Turonian bridge creek limestone member using evolutive harmonic analysis and stratigraphic modeling. *J. Sediment. Res.* **71**, 628–644 (2001).
37. J. Laurin, S. R. Meyers, S. Galeotti, L. Lanci, Frequency modulation reveals the phasing of orbital eccentricity during Cretaceous Oceanic Anoxic Event II and the Eocene hyperthermals. *Earth Planet. Sci. Lett.* **442**, 143–156 (2016).
38. M. L. Machlus, P. E. Olsen, N. Christie-Blick, S. R. Hemming, Spectral analysis of the lower Eocene Wilkins Peak Member, Green River Formation, Wyoming: Support for Milankovitch cyclicity. *Earth Planet. Sci. Lett.* **268**, 64–75 (2008).
39. S. R. Meyers, Resolving Milankovitchian controversies: The Triassic Latemar Limestone and the Eocene Green River Formation. *Geology* **36**, 319 (2008).
40. M. T. Taner, *Attributes Revisted, Technical Report* (Rock Solid Images Inc., 1992).
41. J. Zhu, C. J. Poulsen, J. E. Tierney, Simulation of Eocene extreme warmth and high climate sensitivity through cloud feedbacks. *Sci. Adv.* **5**, eaax1874 (2019).
42. M. Cramwinckel, N. J. Burls, A. A. Fahad, S. Knapp, C. K. West, T. Reichgelt, D. R. Greenwood, W.-L. Chan, Y. Donnadieu, D. Hutchinson, Agatha Margaretha De Boer, J.-B. Ladant, P. Morozova, I. Niezgodzki, G. Knorr, S. Steinig, Z. Zhang, J. Zhu, R. Feng, D. J. Lunt, A. Abe-Ouchi, G. N. Inglis, Global- and regional-scale hydrological response to early Eocene warmth. preprint, Climatology (Global Change) (2022).
43. D. J. Lunt, F. Bragg, W. L. Chan, D. K. Hutchinson, J.-B. Ladant, P. Morozova, I. Niezgodzki, S. Steinig, Z. Zhang, J. Zhu, A. Abe-Ouchi, E. Anagnostou, A. M. de Boer, H. K. Coxall, Y. Donnadieu, G. Foster, G. N. Inglis, G. Knorr, P. M. Langebroek, C. H. Lear, G. Lohmann, C. J. Poulsen, P. Sepulchre, J. E. Tierney, P. J. Valdes, E. M. Volodin, T. Dunkley Jones, C. J. Hollis, M. Huber, B. L. Otto-Bliesner, DeepMIP: Model intercomparison of Early Eocene Climatic Optimum (EECO) large-scale climate features and comparison with proxy data. *Clim. Past* **17**, 203–227 (2021).
44. D. J. Lunt, M. Huber, E. Anagnostou, M. L. J. Baatsen, R. Caballero, R. De Conto, H. A. Dijkstra, Y. Donnadieu, D. Evans, R. Feng, G. L. Foster, E. Gasson, A. S. von der Heydt, C. J. Hollis, G. N. Inglis, S. M. Jones, J. Kiehl, S. K. Turner, R. L. Korty, R. Kozdon, S. Krishnan, J.-B. Ladant, P. Langebroek, C. H. Lear, A. N. Le Grande, K. Littler, P. Markwick, B. Otto-Bliesner, P. Pearson, C. J. Poulsen, U. Salzmann, C. Shields, K. Snell, M. Stärz, J. Super, C. Tabor, J. E. Tierney, G. J. L. Tourte, A. Tripati, G. R. Upchurch, B. S. Wade, S. L. Wing, A. M. E. Winguth, N. M. Wright, J. C. Zachos, R. E. Zeebe, The DeepMIP contribution to PMIP4: Experimental design for model simulations of the EECO, PETM, and pre-PETM. *Geosci. Model Dev.* **10**, 889–901 (2017).

45. N. Herold, J. Buzan, M. Seton, A. Goldner, J. A. M. Green, R. D. Müller, P. Markwick, M. Huber, A suite of Early Eocene (~55 Ma) climate model boundary conditions. *Geosci. Model Dev. Discuss.* **7**, 529–562 (2014).
46. D. J. Lunt, A. Farnsworth, C. Loptson, G. L. Foster, P. Markwick, C. L. O'Brien, R. D. Pancost, S. A. Robinson, N. Wrobel, Palaeogeographic controls on climate and proxy interpretation. *Clim. Past* **12**, 1181–1198 (2016).
47. Z. He, Z. Zhang, Z. Guo, Reconstructing early Eocene (~55 Ma) paleogeographic boundary conditions for use in paleoclimate modelling. *Sci. China Earth Sci.* **62**, 1416–1427 (2019).
48. C. C. Routson, N. P. McKay, D. S. Kaufman, M. P. Erb, H. Goosse, B. N. Shuman, J. R. Rodysill, T. Ault, Mid-latitude net precipitation decreased with Arctic warming during the Holocene. *Nature* **568**, 83–87 (2019).
49. C. C. Routson, M. P. Erb, N. P. McKay, High latitude modulation of the holocene North American monsoon. *Geophys. Res. Lett.* **49**, e2022GL099772 (2022).
50. P. Huybers, C. Wunsch, Obliquity pacing of the late Pleistocene glacial terminations. *Geophys. Res. Lett.* **30**, (2003).
51. A. A. Baczynski, F. A. McInerney, S. L. Wing, M. J. Kraus, J. I. Bloch, R. Secord, Constraining paleohydrologic change during the Paleocene-Eocene Thermal Maximum in the continental interior of North America. *Palaeogeogr. Palaeoclimatol. Palaeoecol.* **465**, 237–246 (2017).
52. P. Vervoort, S. Kirtland Turner, F. Rochholz, A. Ridgwell, Earth system model analysis of how astronomical forcing is imprinted onto the marine geological record: The role of the inorganic (carbonate) carbon cycle and feedbacks. *Paleoceanogr. Paleoclimatology* **36**, e2020PA004090 (2021).
53. T. J. Crowley, K.-Y. Kim, J. G. Mengel, D. A. Short, Modeling 100,000-year climate fluctuations in pre-Pleistocene time series. *Science* **255**, 705–707 (1992).
54. W. F. Ruddiman, *Earth's Climate: Past and Future* (W.H. Freeman and Company, ed. 3, 2014).
55. D. B. Kemp, Shallow-water records of astronomical forcing and the eccentricity paradox. *Geology* **39**, 491–494 (2011).
56. B. S. Cramer, J. D. Wright, D. V. Kent, M.-P. Aubry, Orbital climate forcing of δ^{13}C excursions in the late Paleocene–early Eocene (chrons C_{24n}–C_{25n}). *Paleoceanography* **18**, 1097 (2003).
57. L. J. Lourens, A. Sluijs, D. Kroon, J. C. Zachos, E. Thomas, U. Röhl, J. Bowles, I. Raffi, Astronomical pacing of late Palaeocene to early Eocene global warming events. *Nature* **435**, 1083–1087 (2005).
58. J. C. Zachos, H. McCarren, B. Murphy, U. Röhl, T. Westerhold, Tempo and scale of late Paleocene and early Eocene carbon isotope cycles: Implications for the origin of hyperthermals. *Earth Planet. Sci. Lett.* **299**, 242–249 (2010).
59. V. Lauretano, K. Littler, M. Polling, J. C. Zachos, L. J. Lourens, Frequency, magnitude and character of hyperthermal events at the onset of the Early Eocene Climatic Optimum. *Clim. Past* **11**, 1313–1324 (2015).
60. D. F. Williams, J. Peck, E. B. Karabanov, A. A. Prokopenko, V. Kravchinsky, J. King, M. I. Kuzmin, Lake baikal record of continental climate response to orbital insolation during the past 5 million years. *Science* **278**, 1114–1117 (1997).
61. C. Ma, S. R. Meyers, B. B. Sageman, B. S. Singer, B. R. Jicha, Testing the astronomical time scale for oceanic anoxic event 2, and its extension into Cenomanian strata of the Western Interior Basin (USA). *GSA Bull.* **126**, 974–989 (2014).
62. J. Sha, P. E. Olsen, Y. Pan, D. Xu, Y. Wang, X. Zhang, X. Yao, V. Vajda, Triassic–Jurassic climate in continental high-latitude Asia was dominated by obliquity-paced variations (Junggar Basin, Ürümqi, China). *Proc. Natl. Acad. Sci. U.S.A.* **112**, 3624–3629 (2015).
63. W. Fu, D.-y. Jiang, I. P. Montañez, S. R. Meyers, R. Motani, A. Tintori, Eccentricity and obliquity paced carbon cycling in the Early Triassic and implications for post-extinction ecosystem recovery. *Sci. Rep.* **6**, 27793 (2016).
64. P. E. Olsen, J. Laskar, D. V. Kent, S. T. Kinney, D. J. Reynolds, J. Sha, J. H. Whiteside, Mapping Solar System chaos with the Geological Orrery. *Proc. Natl. Acad. Sci. U.S.A.* **116**, 10664–10673 (2019).
65. V. A. Piedrahita, S. Galeotti, X. Zhao, A. P. Roberts, E. J. Rohling, D. Heslop, F. Florindo, K. M. Grant, L. Rodríguez-Sanz, D. Reghellin, R. E. Zeebe, Orbital phasing of the Paleocene-Eocene thermal maximum. *Earth Planet. Sci. Lett.* **598**, 117839 (2022).
66. J. E. Tierney, F. S. R. Pausata, P. B. deMenocal, Rainfall regimes of the Green Sahara. *Sci. Adv.* **3**, e1601503 (2017).
67. T. Bhattacharya, J. E. Tierney, J. A. Addison, J. W. Murray, Ice-sheet modulation of deglacial North American monsoon intensification. *Nat. Geosci.* **11**, 848–852 (2018).
68. G. Windler, J. E. Tierney, P. N. DiNezio, K. Gibson, R. Thunell, Shelf exposure influence on Indo-Pacific Warm Pool climate for the last 450,000 years. *Earth Planet. Sci. Lett.* **516**, 66–76 (2019).
69. G. Windler, J. E. Tierney, J. Zhu, C. J. Poulsen, Unraveling glacial hydroclimate in the Indo-Pacific warm pool: Perspectives from water isotopes. *Paleoceanogr. Paleoclimatol.* **35**, e2020PA003985 (2020).
70. G. Windler, J. E. Tierney, K. J. Anchukaitis, Glacial-interglacial shifts dominate tropical Indo-Pacific hydroclimate during the late Pleistocene. *Geophys. Res. Lett.* **48**, e2021GL093339 (2021).
71. J. E. Tierney, A. Torfstein, T. Bhattacharya, Late Quaternary hydroclimate of the Levant: The leaf wax record from the Dead Sea. *Quat. Sci. Rev.* **289**, 107613 (2022).
72. S. R. Meyers, Astrochron: An R Package for Astrochronology (2014).
73. R Core Team, R: A Language and Environment for Statistical Computing (R Foundation for Statistical Computing, 2021).
74. D. J. Thomson, Spectrum estimation and harmonic analysis. *Proc. IEEE* **70**, 1055–1096 (1982).
75. M. E. Mann, J. M. Lees, Robust estimation of background noise and signal detection in climatic time series. *Clim. Change* **33**, 409–445 (1996).
76. M. O. Patterson, M. Kay, T. Naish, C. Escutia, F. J. Jimenez-Espejo, M. E. Raymo, S. R. Meyers, L. Tauxe, H. Brinkhuis; IODP Expedition 318 Scientists, Orbital forcing of the East Antarctic ice sheet during the Pliocene and Early Pleistocene. *Nat. Geosci.* **7**, 841–847 (2014).
77. G. P. Weedon, *Time-Series Analysis and Cyclostratigraphy: Examining Stratigraphic Records of Environmental Cycles* (Cambridge Univ. Press, 2003).
78. M. Blaauw, J. Andres Christen, M. A. Aquino Lopez, J. E. Vazquez, Oscar M. Gonzalez V, T. Belding, J. Theiler, B. Gough, C. Karney, rbacon: Age-depth modelling using Bayesian statistics (2022).
79. J. W. Hurrell, M. M. Holland, P. R. Gent, S. Ghan, J. E. Kay, P. J. Kushner, J.-F. Lamarque, W. G. Large, D. Lawrence, K. Lindsay, W. H. Lipscomb, M. C. Long, N. Mahowald, D. R. Marsh, R. B. Neale, P. Rasch, S. Vavrus, M. Vertenstein, D. Bader, W. D. Collins, J. J. Hack, J. Kiehl, S. Marshall, The Community Earth System Model: A framework for collaborative research. *Bull. Am. Meteorol. Soc.* **94**, 1339–1360 (2013).
80. E. Brady, S. Stevenson, D. Bailey, Z. Liu, D. Noone, J. Nusbaumer, B. L. Otto-Bliesner, C. Tabor, R. Tomas, T. Wong, J. Zhang, J. Zhu, The connected isotopic water cycle in the Community Earth System Model version 1. *J. Adv. Model. Earth Syst.* **11**, 2547–2566 (2019).
81. J. Zhu, C. J. Poulsen, B. L. Otto-Bliesner, Z. Liu, E. C. Brady, D. C. Noone, Simulation of early Eocene water isotopes using an Earth system model and its implication for past climate reconstruction. *Earth Planet. Sci. Lett.* **537**, 116164 (2020).
82. D. J. Lunt, A. Ridgwell, A. Sluijs, J. Zachos, S. Hunter, A. Haywood, A model for orbital pacing of methane hydrate destabilization during the Palaeogene. *Nat. Geosci.* **4**, 775–778 (2011).
83. E. A. Jagniecki, T. K. Lowenstein, D. M. Jenkins, R. V. Demicco, Eocene atmospheric CO2 from the nahcolite proxy. *Geology* **43**, 1075–1078 (2015).
84. L. Gao, E. J. Edwards, Y. Zeng, Y. Huang, Major evolutionary trends in hydrogen isotope fractionation of vascular plant leaf waxes. *PLOS ONE* **9**, e112610 (2014).
85. S. J. Feakins, Pollen-corrected leaf wax D/H reconstructions of northeast African hydrological changes during the late Miocene. *Palaeogeogr. Palaeoclimatol. Palaeoecol.* **374**, 62–71 (2013).
86. S. J. Feakins, A. L. Sessions, Controls on the D/H ratios of plant leaf waxes in an arid ecosystem. *Geochim. Cosmochim. Acta* **74**, 2128–2141 (2010).
87. V. F. Schwab, Y. Garcin, D. Sachse, G. Todou, O. Séné, J. M. Onana, G. Achoundong, G. Gleixner, Effect of aridity on δ^{13}C and δD values of C_3 plant- and C_4 graminoid-derived leaf wax lipids from soils along an environmental gradient in Cameroon (Western Central Africa). *Org. Geochem.* **78**, 99–109 (2015).

Acknowledgments: We thank P. Murphy, T. Elpers, R. Cline, and D. Radhi Al Abbas for assistance with sample preparation and measurement and M. E. Smith for the helpful discussions. **Funding:** This work was supported by NSF grants EAR #1812525 to J.E.T. and EAR #1813278 to A.R.C. and S.R.M. This study is also based on work supported by the National Center for Atmospheric Research, which is a major facility sponsored by the NSF under Cooperative Agreement No. 1852977. Computing and data storage resources, including the Cheyenne supercomputer (https://doi.org/10.5065/D6RX99HX), were provided by the Computational and Information Systems Laboratory (CISL) at the National Center for Atmospheric Research (NCAR). **Author contributions:** A.P.W. and J.E.T. designed the study. A.P.W., J.E.T., and K.G. conducted laboratory analyses. J.Z. performed modeling experiments with input from J.E.T. A.P.W., J.E.T., J.Z., S.R.M., K.G., and A.R.C. completed data analysis. All authors contributed to the writing of this manuscript. **Competing interests:** The authors declare that they have no competing interests. **Data and materials availability:** All data needed to evaluate the conclusions in the paper are present in the paper and/or the Supplementary Materials. Additional data related to this paper are available in data tables archived in the NOAA NCEI Paleoclimatology database at https://ncei.noaa.gov/access/paleo-search/study/38021.

Submitted 23 January 2023
Accepted 6 July 2023
Published 4 August 2023
10.1126/sciadv.adg8022

Science Advances

Climate system asymmetries drive eccentricity pacing of hydroclimate during the early Eocene greenhouse

Andrew P. Walters, Jessica E. Tierney, Jiang Zhu, Stephen R. Meyers, Katherine Graves, and Alan R. Carroll

Sci. Adv., **9** (31), eadg8022.
DOI: 10.1126/sciadv.adg8022

Science Advances (ISSN) is published by the American Association for the Advancement of Science. 1200 New York Avenue NW, Washington, DC 20005. The title *Science Advances* is a registered trademark of AAAS.